Inverse Design of Mechanical Metamaterials That Undergo Buckling

Giorgio Oliveri and Johannes T.B. Overvelde*

Metamaterials are man-made materials which get their properties from their structure rather than their chemical composition. Their mesostructure is specifically designed to create functionalities not found in nature. However, despite the broad variety of metamaterials developed in recent years, a straightforward procedure to design these complex materials with tailored properties has not yet been established. Here, the inverse design problem is tackled by introducing a general optimization tool to explore the range of material properties that can be achieved. Specifically, a stochastic optimization algorithm is applied and its applicability to disjoint problems is demonstrated, with a focus on tuning the buckling properties of mechanical metamaterials, including experimental verification of the predictions. Besides this problem, this algorithm can be applied to a large variety of systems that, because of their complexity, would be challenging otherwise. Potential applications range from the design of optomechanical resonators, acoustic band gap materials, to dielectric metasurfaces.

1. Introduction

Metamaterials are materials that derive their properties from their structure, not only from their chemical composition. The microstructure of these materials is specifically designed to create new functionalities not found in nature, such as materials characterized by a negative index of refraction,[1,2] negative Poisson's ratio,[3] and a very high stiffness to weight ratio,[4] or structures that enable optical[5] and mechanical[6] cloaking. While most of the properties of these metamaterials are fixed, compliance, resulting from the use of soft or relatively thin materials, can be used as a paradigm to design reconfigurable metamaterials with tunable functionality. Applications range from materials with adaptive auxetic behavior,[7–10] tunable stiffness,[11] or ad-hoc optical,[12,13] phononic,[14,15] and acoustic[16] properties, to tunable surface properties such as the drag coefficient,[17] wettability,[18] and chemistry.[19]

A particularly interesting avenue has been to harness mechanical instabilities in the design of reconfigurable metamaterials, which changes the continuous nature of the

transformation to a discrete response originating from bifurcation. Interestingly, these instabilities can be used to increase the sensitivity to external loads, and enable multistability and hysteretic behavior.[20] In contrast to the complex and unstable behavior that these mechanical metamaterials show, their architecture is often surprisingly simple. One of the iconic examples is an elastomeric material patterned with a square lattice of circular pores.[7] Upon compression, a collective buckling instability suddenly changes the Poisson's ratio from positive to negative, and in a similar fashion changes the phononic behavior by opening and closing band gaps.[14] While several studies focused on the effects of pore shape,[9] pore distribution[21] and material loading direction,[22] the mechanical properties have only been tuned within limits dictated by a few geometrical parameters. Here, design optimization approaches could play a key role in solving the inverse problem to design mechanical metamaterials with specific properties, and explore the bounds of achievable functionality.

A specific inverse design approach that has been successfully applied to a large variety of problems is called topology optimization. This method has been developed to allow for complete design freedom by varying the local density of the structure, and therefore does not require a description and parametrization of the geometry beforehand.[23] While topology optimization was initially used to solve mechanical design problems such as maximizing structural stiffness using a limited amount of material,[24–26] it gradually expanded towards other research areas such as optics,[27–30] phononics,[31] material science,[32–34] and fluid mechanics.[35] Importantly, most of the algorithms use gradient information of the objective function and constraints to reach a local or global minimum. Therefore, the optimization problem needs to be continuous and differentiable with respect to the design variables. While some work has been done to include buckling behavior in the optimization problem either through constraints[36] or the objective function,[26,37] the requirement of gradient information in the applied methods complicates the applicability and generalization of these approaches for more nonlinear problems. Moreover, the presence of multiple local minima makes the optimization highly dependent on the initial conditions[38] and search algorithm. Besides these gradient-based methods, other approaches to optimize the behavior of mechanical networks exist, including stochastic optimization approaches[39,40]

G. Oliveri, Dr. J. T. B. Overvelde
AMOLF
Science Park 104, 1098 XG Amsterdam, Netherlands
E-mail: overvelde@amolf.nl

The ORCID identification number(s) for the author(s) of this article can be found under https://doi.org/10.1002/adfm.201909033.

and evolutionary approaches that are inspired by mechanical allostery.[41,42]

Here, we apply stochastic optimization to design the buckling response of periodic structures, in which the objective functions do not require objective function differentiability. To reduce the search space and to generate smooth structures, we introduce a heuristic subroutine inspired by the ferromagnetic Ising model. In order to determine the effectiveness of such an approach, we reduce computational time by considering the linear buckling response, such that we can perform multiple optimizations and compare their results (i.e. >500 solutions per objective). More specifically, we show how it is possible to design structures with maximum buckling load, but also allow tailoring to a predefined buckling force within a wide range of values. We furthermore show that by controlling the occurrence of higher modes, we can effectively remove multi-mode interactions that occur for nearly degenerate bifurcations. Finally, we validate our optimized designs using compression experiments on elastomeric samples. While the performances of gradient based topology optimization algorithms have been proven to be unmatched,[38] here we show that stochastic algorithms, due to their flexibility and relative simplicity of implementation, provide a general approach beneficial to explore more complex problems.

1.1. Problem Description

To emphasize how the morphology of a structure can alter its buckling behavior in a discontinuous fashion, we performed a buckling analysis on a range of beams with different pore shape. Each beam is composed of $n = 10$ vertically placed square unit cells that contain a pore defined by a geometrical parameter c. The radius of the pore shape is defined as [9]

$$r(\theta) = \frac{L\sqrt{2\phi}}{\sqrt{\pi(2 + c^2)}}\left[1 + c\cos(4\theta)\right] \tag{1}$$

in which $0 \leq \theta \leq 2\pi$, L is the size of the unit cell, and ϕ the porosity. We applied a vertical compressive strain on beams with a porosity $\phi = 0.5$ and ran linear buckling analyses for $-0.1 \leq c \leq 0.1$ using the Finite Element Analysis (FEA) package Abaqus, in which we discretized the structure using biquadratic plane stress elements (CPE8R). In **Figure 1**, we show the critical strain ϵ^{cr} for the first 20 buckling modes as a function of the pore shape. By monitoring the displacement of 11 nodes along the longitudinal axis of the beams, we were able to correlate the mode shape between the different beams via bivariate correlation.[43] This enables us to identify mode switching that arises from changes in pore geometry.

We next focus on the buckling mode with the lowest critical strain, since this mode will occur upon compression of the beam. We find that for $c < 0.075$, the buckling mode of the beam is characterized by a typical macroscopic buckling mode with a wavelength of $2nL$ that is equal to twice the length of the beam, while for $c > 0.075$ a microscopic buckling mode occurs characterized by a wavelength of $2L$ equal to twice the size of the unit cell.[44,45] When we would perform an optimization to maximize the lowest critical strain of the beam according to

$$\max_{c} \quad \epsilon_1^{cr} \tag{2}$$

we find that the derivative of the objective function $d\epsilon_1^{cr}/dc$ is discontinuous due to the change in buckling behavior (Figure 1). While this specific problem can be tackled with gradient-based algorithms by rewriting Equation (2) using a bound formulation,[37,46] a perturbation-based sensitivity analysis should be performed for each individual eigenvalue by solving sub-optimization problems at each optimization step. For the specific case shown in Figure 1 in which the optimal solution lies exactly at the point where the first two modes switch order, gradient-based methods would require taking progressively smaller steps in the proximity of mode swaps in order to guarantee smoothness. This, together with the difficulties
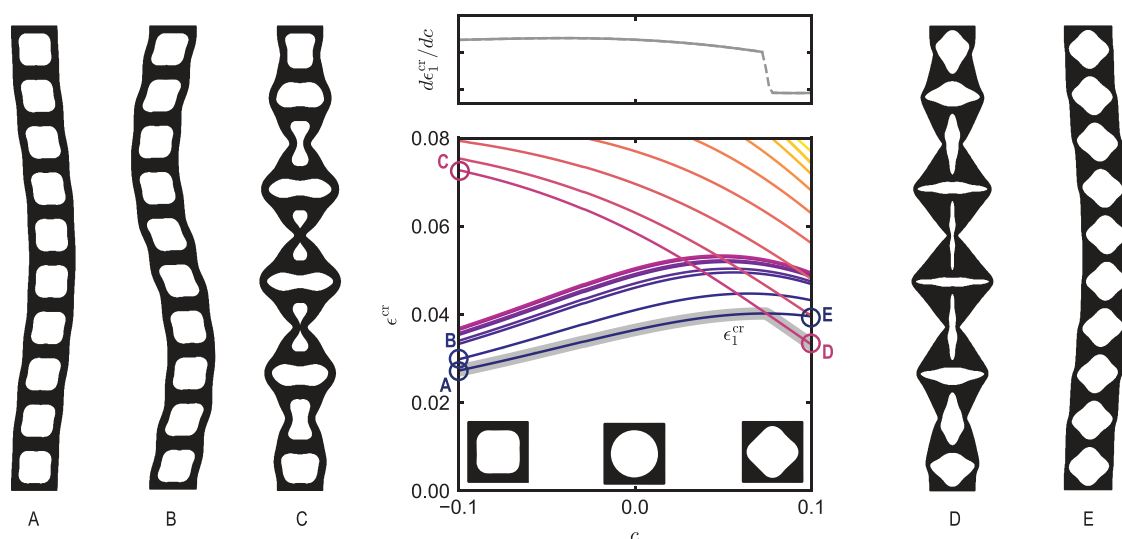

Figure 1. FEA simulation results showing the effect of pore shape on the buckling behavior of periodic porous beams under vertical compression. Here the first twenty modes are shown. Since mode switching occurs at $c = 0.075$, the buckling strain of the first mode ϵ_1^{cr} is not continuously differentiable, such that gradient-based optimization algorithms cannot be applied to optimize buckling behavior.

associated with tuning for a specific target buckling value ϵ_1^{cr}, strengthens the need of optimization techniques that do not rely on gradient information to seek the optimum.

2. Stochastic Optimization

In order to find structures with interesting and specific buckling behavior, we developed a density-based stochastic topology optimization approach based on the geometrical description used in the SIMP interpolation method.[47,48] The topology of the structure, which is divided into square elements, can be changed by varying the density of the elements between $0 \leq \rho_i \leq 1$. Differently, in our stochastic optimization implementation, we can use a discrete representation of the design since we do not require intermediate unrealistic densities to make our design continuously differentiable.[39] As such, we assume that each element can take a density ρ_i of $\rho_{min} \approx 0$ (void) or $\rho_{max} = 1$ (solid). When assuming linear elastic behavior of each element, we can evaluate the initial mechanical and buckling response of the structures by using a linear FEA code implemented in Matlab (details in Section S1, Supporting Information), in which the stiffness and Poisson's ratio of each element are given by $E_i = \rho_i E$ and $\nu_i = \rho_i \nu$ to account for the geometry of the structure.

Starting from an initial random density distribution with a solid/void ratio of ϕ, we alter the geometry by randomly picking and exchanging two elements with different density. After each change in geometry, the objective function $\Phi(\rho_i)$ is evaluated. Following a simulated annealing optimization approach,[49] the variation in objective function $\Delta\Phi(\rho_i)$ between current and previous iteration is used to determine the acceptance probability, $P(\Delta\Phi(\rho_i))$ of the new candidate solution according to

$$P\left(\Delta\,\Phi(\rho_i)\right) = e^{\frac{\Delta\,\Phi(\rho_i)}{T}} \tag{3}$$

where T is a parameter often referred to as the temperature, which can be used to tune the acceptance probability of optimization steps that do not improve the objective function, in order to reach global optima. Here, we use a fixed number of iterations for the optimization, N_{iter}, and assume an exponential decay of the temperature.[49,50] We let the temperature decrease from T_{max} to T_{min}, such that the temperature at a given iteration n is given by

$$T(n) = T_{max}\left(\frac{T_{min}}{T_{max}}\right)^{n/N_{iter}} \tag{4}$$

2.1. A Test Problem: Compliance Optimization

While our main goal is to optimize buckling behavior, we will first test our method using a typical topology optimization problem that is computationally less expensive. We focus on compliance optimization (i.e., stiffness maximization), and do this by replicating the MBB-beam optimization problem[51,52] (see schematic in **Figure 2**a). This allows us to compare our implementation with previous work. If we consider a domain with $n_x \times n_y = 60 \times 20$ elements, the optimization problem can be formulated as

$$\min_{\rho_i} \quad \Phi(\rho_i) = C = \{\boldsymbol{D}\}^T[\boldsymbol{K}]\{\boldsymbol{D}\} \tag{5a}$$

$$s.t. \quad \{\boldsymbol{F}\} = [\boldsymbol{K}]\{\boldsymbol{D}\} \tag{5b}$$

$$\frac{V_{solid}}{V_{\Omega}} = \phi^* = 0.5 \tag{5c}$$

where $\{\boldsymbol{D}\}$ and $\{\boldsymbol{F}\}$ are vectors containing the displacement and reaction forces at the nodes, respectively, which are related by the stiffness matrix $[\boldsymbol{K}]$ (see Section S1, Supporting Information). Moreover, the volume constraint of Equation (5c) enforces that the ratio between the volume of material elements, V_{solid}, and the total domain volume, V_{Ω}, is constant. Note that in our approach, this volume constraint is automatically satisfied, and depends on the initial solid/void fraction. Finally, we normalize the compliance of our designs C by the compliance of a homogeneous structure C_{ref} with $\rho_i = 0.5$, such that $\tilde{C} = C/C_{ref}$.

We start by identifying proper temperature bounds (T_{max} and T_{min}) for the simulated annealing algorithm (Equation (4)). First, to determine the objective function sensitivity to the temperature, we run ten optimizations with a total number of iterations equal to $N_{iter} = 1.5 \times 10^4$, during which the temperature is decreased according to Equation (4) between $T_{max} = 10^2$ and $T_{min} = 1 \times 10^{-9}$. By looking at the objective function evolution for decreasing T (Figure 2a), we identify three regimes. i) For high temperatures ($T > 20$) any candidate solution is accepted, such that the objective function fluctuates around the same value and there is no convergence to an optimum. ii) Intermediate temperatures ($1 \times 10^{-7} \leq T \leq 20$) result in convergence toward a minimum, with a probability to reach a global minimum. iii) For $T < 1 \times 10^{-7}$, only candidate solutions with lower objective function are accepted; the algorithm behaves as a random search with steepest descent and therefore only converges to a local minimum. For optimal behavior of the simulated annealing algorithm, we focus on regime (ii), such that $T_{max} = 20$ and $T_{min} = 1 \times 10^{-7}$.

Using these specific bounds for the temperature, we next focus on finding the required number of iterations N_{iter}. To do so, we performed several optimizations with $500 \leq N_{iter} \leq 15000$. In Figure 2b, we show the final objective function values for 30 optimizations per data point. As expected, we find that a larger number of iterations (i.e., a slower cooling rate) benefits the objective function optimization. This can also be seen by looking at the topologies associated with different cooling rates (Figure 2b), which become more clustered given enough time. Balancing the time required for the optimization with the final objective function value, $N_{iter} = 10^4$ seems to be a good choice for the number of iterations, for which the typical $\tilde{C} \approx 0.9$.

3. Ising-Inspired Subroutine

As can be seen from the compliance optimization examples (Figure 2b), while the solutions are converging, the current approach leads to structures with fragmentation and local checkerboard patterns. This is a typical problem in topology
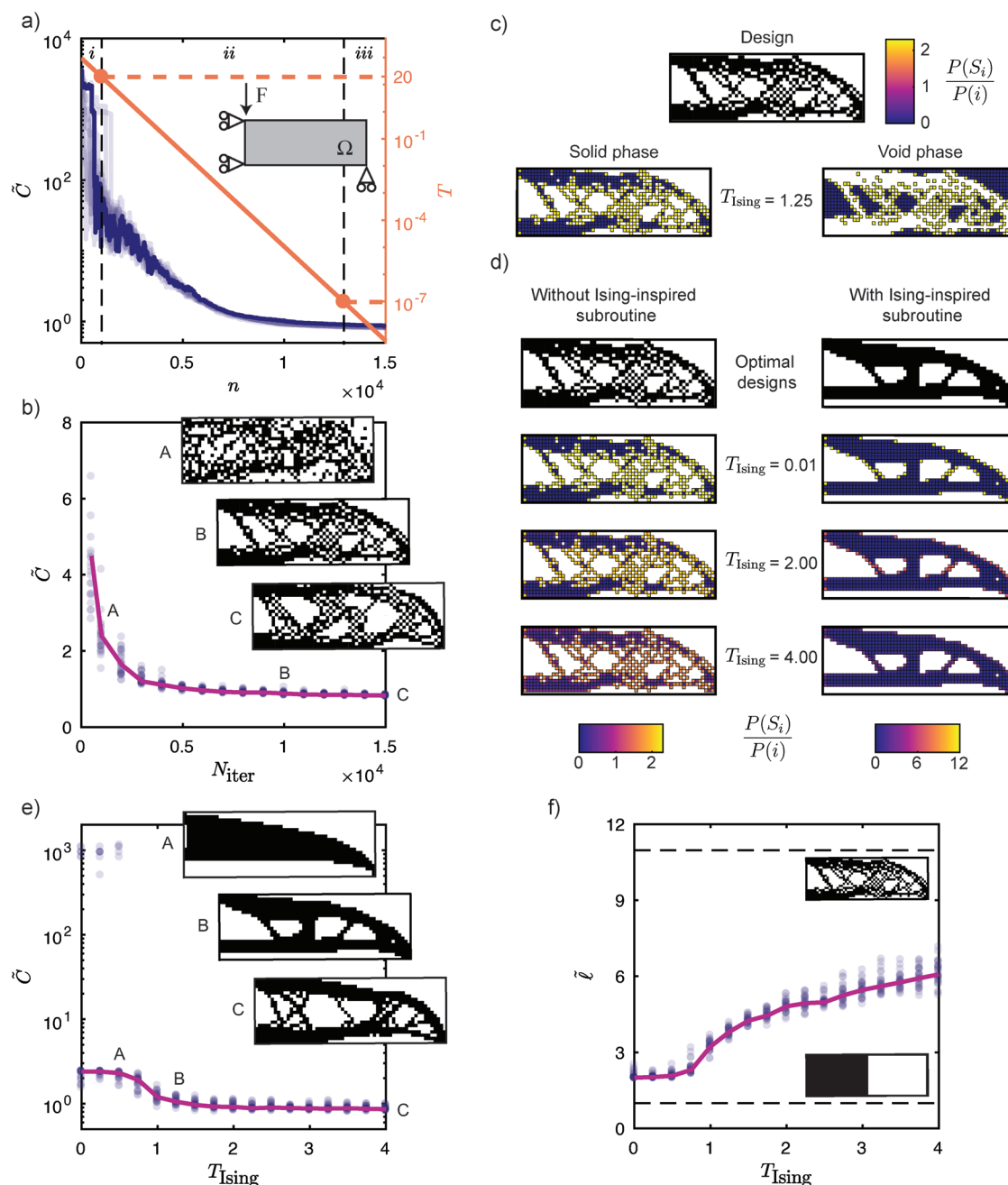
**ADVANCED
SCIENCE NEWS**
www.advancedsciencenews.com

**ADVANCED
FUNCTIONAL
MATERIALS**
www.afm-journal.de

Figure 2. Compliance optimization of the MBB-beam problem using our stochastic optimization algorithm without and with Ising-inspired subroutine. a) Selecting the optimal temperature bounds (T_{max} and T_{min}) for the simulated annealing algorithm for actual optimization runs by performing ten different optimizations. b) Dependency of the final optimized solutions on the number of iterations N_{iter}. For each value of N_{iter}, 30 optimizations have been performed, where the insets show one of the final optimized solutions for $N_{iter} = 10^3$, 10^4 and 1.5×10^4. c) Probability distribution of the Ising-inpired subroutine to change the density of an element as determined from Equation (9) within a solid or void phase, relative to the optimal solution B in Figure 2b. d) Effect of Ising temperature on the swapping probability of elements in the solid phase for optimized solutions found without and with the Ising-inspired subroutine. e) Dependency of the final optimized solutions on the Ising temperature T_{Ising}. For each value of T_{Ising}, 30 optimizations have been performed, where the insets show one of the final optimized solutions for $T_{Ising} = 0.5$, 1.25, and 4. f) Length of the material-void interface for the optimized solutions. The insets represent the bounds for the length.

optimization, and is the result of artificial stiffening.[53,54] As a result, the optimized geometries highly depends on the choice of mesh density. Moreover, apart from introducing numerical artifacts, these local patterns make the fabrication impossible.

Typically, this problem is solved by introducing local averaging,[55] which is not suitable for our optimization given that we do not take into account intermediate densities. Differently, for discrete grids, a potential solution to overcome checkerboard patterns is, for example, by introducing additional

**ADVANCED
SCIENCE NEWS**
www.advancedsciencenews.com

**ADVANCED
FUNCTIONAL
MATERIALS**
www.afm-journal.de

constraints on the local connectivity of material elements during each step of the optimization[56,57] or by removing the checkerboard pattern by random perturbations during a finite number of the optimization iterations.[39] These methods however only prevent checkerboard patterns, or loosely connected structures, and it is not possible to control more global features in the final optimized structures such as interface length or other feature sizes. Therefore, we introduce an approach to heuristically reduce the probability of certain geometrical features by drawing only specific candidate solutions. Here, we take inspiration from the 2D ferromagnetic Ising Model,[58,59] and implement a subroutine to prioritize clustering of the material, as it is well known that for the Ising model the interface length can be tuned by varying the Ising temperature. While the Ising model describes the behavior of a system formed by magnetic dipole moments of different spins interacting among each other, we translate the spin diversity into material diversity. If we relate the spin to the density of each element according to $s_i = 2\rho_i - 1$, using the Von Neumann neighborhood, the total energy in our system can be written as

$$E = -\frac{1}{2} \sum_{i=1}^{N_{elem}} s_i \left[s_{up(i)} + s_{down(i)} + s_{left(i)} + s_{right(i)} \right] \tag{6}$$

where the spin of each element s_i is only affected by the spins of the four adjacent elements. Therefore, if an element of a certain spin s_i is inverted, the system will experience a variation in Ising energy equal to

$$\Delta E_i = 2 s_i \left[s_{up(i)} + s_{down(i)} + s_{left(i)} + s_{right(i)} \right] \tag{7}$$

which, according to the 2D Ising method, is only accepted with a probability equal to

$$P(\Delta E_i) = e^{-\frac{\Delta E_i}{T_{Ising}}} \tag{8}$$

Here, the Ising temperature T_{Ising} can be used to tune the acceptance probability of certain topological variations. Lower T_{Ising} will result in the formation of more clustered candidate solutions, while higher T_{Ising} will not have much effect on the selection of the candidate solution and therefore will result in topologies similar to those shown in Figure 2b.

Note that for the Ising model, especially for low temperatures, it often occurs that no spin changes are made during a step. To make sure that our design changes in each iteration step, we instead draw an element from the probability distribution specified by

$$P(S_i) = \frac{P(\Delta E_i)}{\sum\limits_{k=1}^{N_{elem}} P(\Delta E_k)} \tag{9}$$

which depends on how the Ising acceptance probability of an element $P(\Delta E_i)$ relates to the total acceptance probability $\sum\limits_{k=1}^{N_{elem}} P(\Delta E_k)$ of the current state. To ensure that the volume constraint is satisfied, each design change is divided into two steps in which we first draw a solid element, update the density and probability distribution, and then we draw a void element. In

Figure 2c, we show the material and void probability distributions of an optimized design with a checkerboard pattern, in which the density distributions are normalized with respect to the probability of a random element selection $P(i)$ (i.e., without using the Ising-inspired subroutine). Moreover, in Figure 2d, we show the effect of T_{Ising} on the probability of making a solid element void for the given configuration. We observe that for low T_{Ising}, the elements located at the solid-void interface (e.g. checkerboard regions) have a high probability of being swapped, while the elements within homogeneous regions have almost zero probability. Increasing the temperature will increase the probability of selecting elements within the homogeneous regions, which in the limit of $T_{Ising} \to \infty$ results in a fully random selection not influenced by the Ising-inspired subroutine.

We next apply this subroutine to the same compliance optimization problem considered previously, using the same parameters for the simulated annealing algorithm, and study the effect of T_{Ising} on the optimized topology. We do so by running 30 simulations per T_{Ising} value. As can be seen in Figure 2e, for low T_{Ising}, the material clusters dramatically and prevents full exploration of the design space. As a result, the optimized designs have a relatively high compliance of $\tilde{C} \approx 2.4$. Moreover, for $T_{Ising} < 0.5$, we find that some optimized designs are disconnected from the boundary conditions (i.e., connected via low-density elements), leading to very high objective values of $\tilde{C} \approx 10^3$. Better results are obtained for $T_{Ising} \geq 1$, for which all the optimizations converge to similar objective function values of $\tilde{C} \approx 0.9$, comparable to the results obtained without Ising-inspired subroutine.

Interestingly, while the objective functions for $T_{Ising} > 1$ found with our stochastic optimization approach are similar, the optimized topologies depend greatly on T_{Ising}. Two examples for which we have used $T_{Ising} = 1.25$ and $T_{Ising} = 4$ are shown in Figure 2e. Clearly, lower T_{Ising} results into more clustered solutions and mitigates the checkerboard patterns, while high T_{Ising} creates thin material connections with sharp material–void interfaces affected by numerical errors. This effect of T_{Ising} on the topology can be shown by considering the final length $\tilde{\ell} = \ell / \ell_{min}$ of the solid–void interface as shown in Figure 2f, where the lower dashed line represents the minimum length ℓ_{min} the given domain can achieve, and the upper dashed line is the length of the optimal design obtained without the Ising-inspired subroutine shown in Figure 2c. For $T_{Ising} > 1$, we find a direct relation between the Ising temperature and the interface length. Similarly, we counted the number of edges that each material element has (Figure S1, Supporting Information) and find that for $T_{Ising} < 1$, the number of elements with two or less neighbors (i.e., which are needed for checkerboard patterns) remains below 7%. Taking both effects into account, we select $T_{Ising} = 1.25$ as the temperature in the following studies. Note, that the results obtained for $T_{Ising} = 1.25$ are ≈30% higher, and therefore not as good as the optimal material distribution obtained with the SIMP method[52] (see Section S3, Supporting Information).

Furthermore, besides reducing the interface length and removing checkerboard patterns, introducing the Ising-inspired subroutine heuristically reduces the number of candidate solutions that are considered during each iteration of the optimization. This is shown in Figure 2d, where we plot the probability of

ADVANCED
SCIENCE NEWS
www.advancedsciencenews.com

ADVANCED
FUNCTIONAL
MATERIALS
www.afm-journal.de

selecting elements of an optimal design obtained with the Ising-inspired subroutine. Notice how the elements with high probability of being swapped are mostly at the material–void interface. Therefore, the optimization first explores the interesting part of the design space, associated with the material interface rather than considering the full domain at each iteration.

4. Buckling Behavior Optimization

The strength of our algorithm becomes visible when dealing with disjoint problems, where conventional gradient-based approaches fail, have a limited versatility, or complicate the implementation. In this section, we will focus on determining the topology of a periodic structure that undergoes buckling. We focus on a beam-like domain composed of $n_x^{uc} \times n_y^{uc} = 2 \times 10$ unit cells, in which each unit cell is made of $n_x \times n_y = 20 \times 20$ elements that are used as the design variables. We fix the top and bottom of the beam and apply a vertical compression. Moreover, to better estimate the bifurcation buckling, we impose mirror symmetry with respect to the vertical axis for the density distribution[60] (see schematic in **Figure 3**a).

4.1. Optimizing for a Specific Buckling Load

We start by determining the optimal topology of the periodic beam for a predefined buckling load. Given a target critical force, the optimization problem can be defined as

$$\min_{\rho_i} \quad \Phi(\rho_i) = \sqrt{(\lambda_1 - \lambda_{1T})^2} \tag{10a}$$

$$s.t. \quad ([K] - \lambda[K_\sigma])\{\delta D\} = \{0\}, \quad \{\delta D\} \neq \{0\} \tag{10b}$$

$$\lambda = \{\lambda_1, \lambda_2, \ldots, \lambda_n\}^T \tag{10c}$$

$$\frac{V_{\text{solid}}}{V_\Omega} = \phi^* = 0.5 \tag{10d}$$

where λ_1 is the first eigenvalue, λ_{1T} is the target eigenvalue, and $[K]$ and $[K_\sigma]$ are the stiffness matrix and the geometrical stiffness matrix, respectively (see Section S1, Supporting Information). The eigenvalues λ are coefficients proportional to the buckling force of the structure. Note that we consider only positive eigenvalues related to compression of the beam, and ignore negative eigenvalues related to tension. Moreover, while here we used $\Phi(\rho_i) = \sqrt{(\lambda_1 - \lambda_{1T})^2}$ for our objective function, similar results might be obtained by using $\Phi(\rho_i) = (\lambda_1 - \lambda_{1T})^2$, although this would affect the specific temperatures that need to be set for the optimization. Furthermore, by performing the same parameter study as done in previous sections for the compliance optimization problem, we obtain suitable temperatures for this problem given by $T_{\max} = 0.01$, $T_{\min} = 10^{-8}$, and $N_{\text{iter}} = 3000$. Finally, we use $T_{\text{Ising}} = 1.25$ as determined previously.

In Figure 3a, we show the results of 900 optimizations for $\tilde{\lambda}_{1T} = \lambda_{1T}/\lambda_{\text{ref}}$ in the range [0.2,3], where λ_{ref} is the first buckling load of a solid beam with equal volume fraction ϕ^*. We find that our algorithm can consistently optimize for targeted buckling forces up to $\tilde{\lambda}_{1T} \approx 1.3$ (i.e., the buckling force is improved by 30% with respect to a solid beam made with the same mass), where we find that approximately 1% of simulations converge to a load different than the objective. Interestingly, for each target buckling force, we find multiple optimal solutions, as shown by the examples in Figure 3b. However, for $\tilde{\lambda}_{1T} > 1.3$ (i.e., $\tilde{\lambda}_1 > 1.3$), we see an increase in diversity, resulting from solutions that do not converge to the target objective. In fact, these solutions are likely the result of optimizations that converge to local minima. Note that for $\tilde{\lambda}_{1T} > 2$ we find that all solutions converge to a value lower than the target, with a median value at $\tilde{\lambda}_1 \approx 1.8$.

4.2. Maximizing Buckling Load

To understand whether the maximum buckling load we achieved for this domain is $\tilde{\lambda}_1 \approx 2$ as we showed in the previous section, or that this limit is an artefact of the convergence to local minima, we next introduce an optimization problem to maximize the
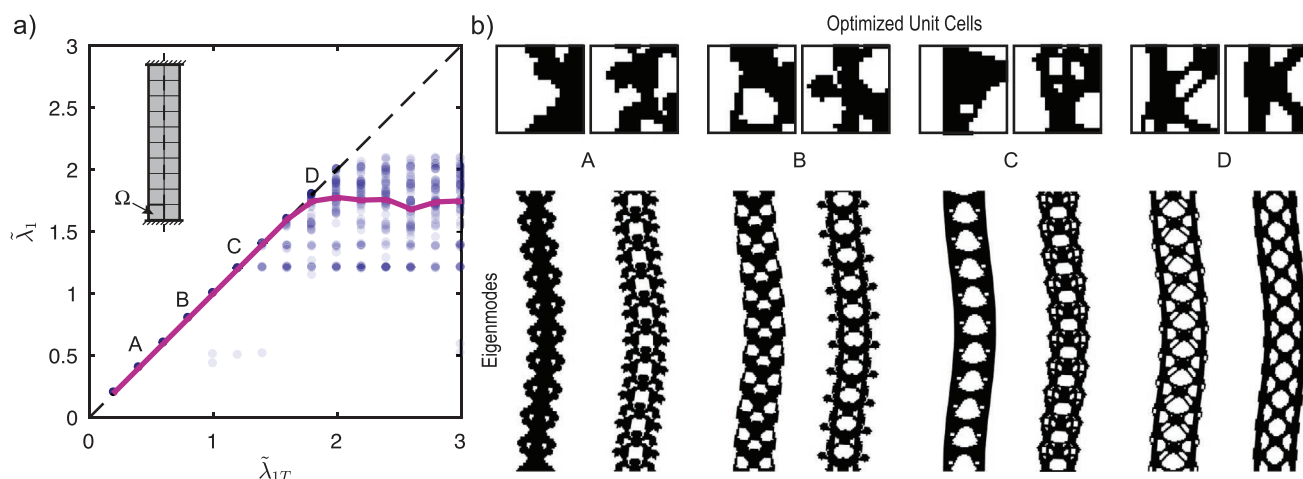

Figure 3. Optimization to a target buckling load $\tilde{\lambda}_{1T}$. a) Results of 900 optimizations (60 per selected $\tilde{\lambda}_{1T}$) as a function of the target value $\tilde{\lambda}_{1T}$. b) Selection of optimal density distributions and the corresponding buckling modes for $\tilde{\lambda}_{1T} = 0.4, 0.8, 1.2,$ and 1.8.

buckling load. This is achieved by setting the target objective buckling force in Equation (10a) to an arbitrarily high value of $\tilde{\lambda}_{1T} = 10$, which effectively will never be reached. Movies 1 and 2, Supporting Information, show the accepted candidate solutions of two optimizations, with and without Ising-inspired subroutine, respectively. It is important to note that during both optimization paths we encounter buckling modes of different wavelengths, indicating the disjoint nature of the problem.

We perform 600 optimizations, each starting from different random initial configurations. The results are shown in **Figure 4**a, in which we plot the normalized buckling force $\tilde{\lambda}_1$ and average moment of inertia $\tilde{I} = \langle I \rangle / \langle I_{ref} \rangle$ for each optimized beam, where $\langle I \rangle = \iiint \rho_i x_i^2 dA\, dy$. As expected, we find that most of the results are clustered within a few local minima indicated by points A-H in Figure 4a. Representative topologies for these local minima are shown in Figure 4b. We find that in order to achieve higher buckling force, the material distribution needs to maximize the moment of inertia, which follows Timoshenko beam theory.[61] As a consequence, an increase in buckling force lowers the stiffness of the structures as shown in the inset of Figure 4a. For beams with lower moment of inertia (e.g., beams A-F), we find that all optimized beams buckle with a wavelength equal to $2n_y^{uc}L$. However, we also observe solutions (e.g., beams G-H) in which the first buckling mode has a wavelength equal to double the size of the unit cell ($2L$), similar to the observation made in Figure 1. This is the result of widening of the beams, which has a direct impact on the thickness and buckling behavior of the internal features. By performing centroid linkage hierarchical clustering on the eigenvector results,[62] we are able to assess the wavelengths of optimized beams, and distinguish beams with wavelengths equal to $2n_y^{uc}L$ from $2L$ as indicated by using blue and pink markers in Figure 4a. The appearance of these two modes seems to limit the maximum buckling load that can be achieved, and we find a maximum buckling load equal to 2.04 times that of a solid beam with the same weight.

4.2.1 Experimental validation

To quantify how the optimized topologies (A-H in Figure 4b) compare with experiments, we fabricated the beams using an elastomeric rubber (Zhermack Elite Double 8). Each beam was casted in a single step in a 3D-printed mold (Stratasys Eden260VS), and has a thickness of 40 mm and a nominal length of 140 mm, associated with a unit cell dimension of 14 × 14 mm. We then performed five compression cycles at a rate of 30 mm min^{-1} to a maximum compression of 20 mm using a materials testing machine (Instron 5965L9510). From the force–displacement response, we can then determine the buckling point F^{cr}, which is found at the intersection between the regression lines of the force–strain curves at small strain $\varepsilon \approx 0$ and right after buckling as indicated by the sharp transition (Figure S3a, Supporting Information). To be able to compare the results with experiments we normalize each response by the experimental buckling force of the reference geometry (solid vertical beam), that is, $\tilde{F} = F/F_{ref}^{cr}$.

The results are summarized in Figure 4c, where we show the difference between the experimental buckling force $\tilde{F}_{cr}$ and

simulation results $\tilde{\lambda}_1$ in function of the normalized moment of inertia of the structures $\tilde{I}$. While beam A, which is closest to a solid beam, is in agreement with the simulation results, wider beams with a more defined porous structure start to show higher buckling forces compared to the numerical results. Interestingly, for beams A-E, we see an approximately linear deviation from the predicted buckling load $\tilde{\lambda}_1$ for increasing $\tilde{I}$. This is likely due to the relatively large strains that need to be applied before the beams buckle (i.e., up to $\varepsilon = 0.12$), such that the beams considerably widen and shorten, resulting into an effective increase in the experimental buckling load. To limit the computation time in our simulations, these nonlinear geometrical effects have not been taken into account in the model.

However, to make sure that the deviation between theory and experiments is due to nonlinear effects, we performed additional nonlinear FEA to determine the buckling load of the optimized 2D beams under plane stress conditions. Note that we have used the same mesh as in our optimization, except for the low-density elements that we removed for the nonlinear analysis. As indicated in Figure 4c, we find that nonlinear effects such as bulging indeed seem to increase the moment of inertia of the beam, resulting in higher buckling loads. However, the obtained results do not fully agree with the experiments, in which we see an even larger increase in the buckling load. This could be the effect of additional geometrical effects that arise in the fully 3D samples. However, additional effects could also play a role, such as differences in boundary conditions, misalignment of the sample, imperfection (or, e.g., increase in ligament thickness) due to the fabrication process, viscoelastic behavior of the material, or numerical effects related to the mesh density.

Finally, this nearly linear relation between buckling force and moment of inertia does not hold for beams F-H. To determine where this deviation is coming from, we show in Figure 4d the experimentally obtained buckled states for all beams right after buckling has occurred. While for beams A-E the beams all buckle in the predicted buckling mode, for beams F-H, we observe a localization of the mode and a sudden drop in force (Figure S3a, Supporting Information). This localization indicates a creasing instability,[63] and is also observed in the nonlinear FEA (Figure S4, Supporting Information). Note that beams D-E also show a similar localization later along the loading path, and therefore undergo a second instability during loading. Importantly, it seems that due to the increase in buckling load of the predicted buckling mode, a mode switch occurs in beams F-H, such that for higher values of the moment of inertia the expected buckling load can no longer be reached.

The sensitivity of the buckling mode to the finite size deformations that occur during loading suggests that the critical values of higher modes are not well separated from the first mode. In **Figure 5**, we show the difference between the critical force of the first and second mode $\tilde{\lambda}_2 - \tilde{\lambda}_1$, as a function of the moment of inertia $\tilde{I}$. Interestingly, we find sudden transitions at $\tilde{I} = 3$ that separates structures that have a well-defined first mode (e.g., A-E) and structures for which multiple modes happen at the same critical force (e.g., F-H). Note that all the structures that exhibit potential microscopic buckling (i.e., have a buckling wavelength of $2L$ as indicated by the pink marker in Figure 5) lay on $\tilde{\lambda}_2 - \tilde{\lambda}_1 \approx 0$, such that we were not able to obtain such a localized mode experimentally.

**ADVANCED
SCIENCE NEWS**

www.advancedsciencenews.com

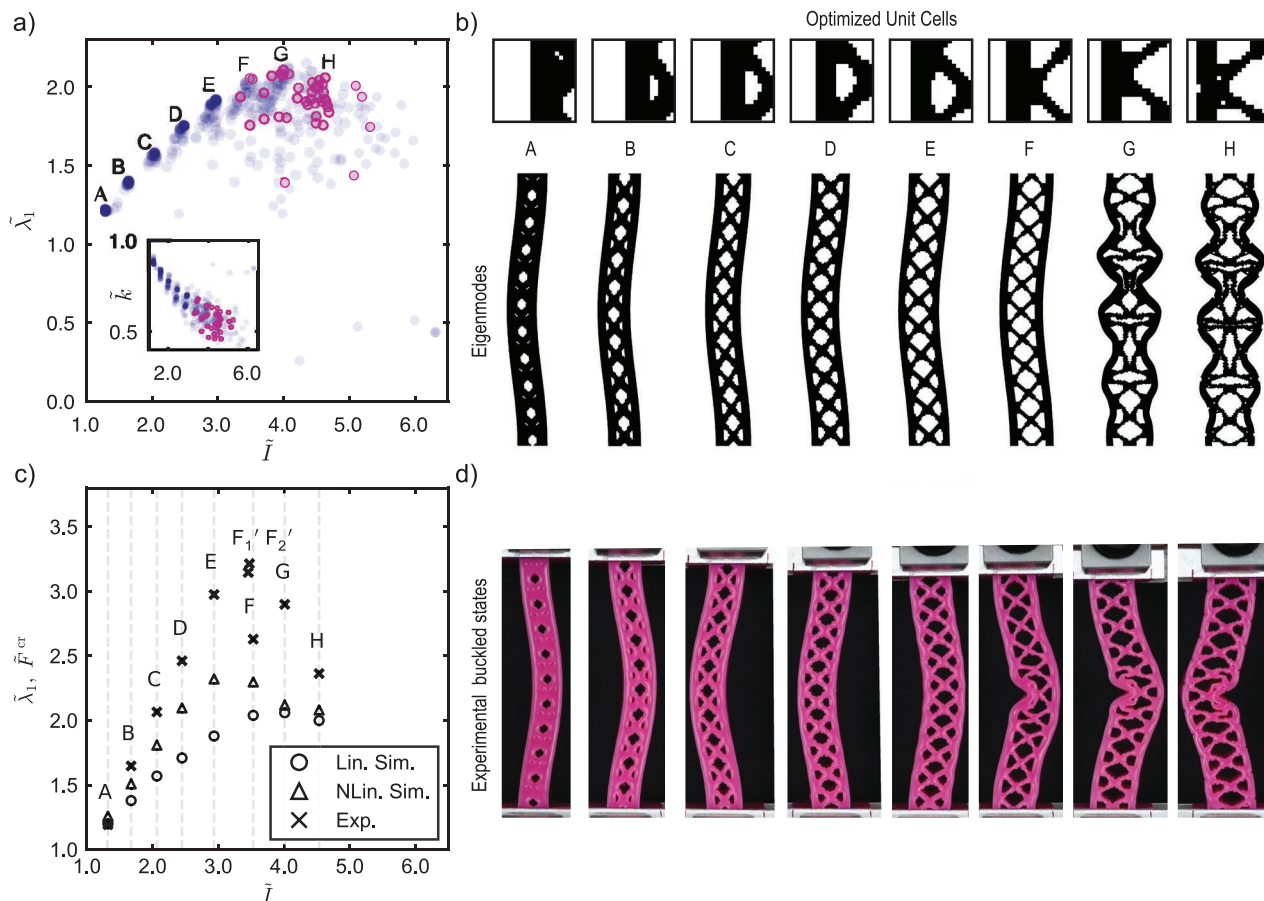**ADVANCED
FUNCTIONAL
MATERIALS**

www.afm-journal.de

Figure 4. Maximum buckling load optimization. a) The buckling load $\tilde{\lambda}_1$ of 600 optimization in function of the optimized structures' normalized moment of inertia $\tilde{I}$. Structures with first modes characterized by long ($2n_y^{uc}L$) or short ($2L$) wavelengths are indicated by the blue and pink markers, respectively. The insets show the effective stiffness $\tilde{k}$ of the optimized solutions. b) Representative unit cells and buckling modes of structures A–H. c) Comparison between prediction of critical buckling load found with linear and nonlinear simulations ($\tilde{\lambda}_1$) and experiments ($\tilde{F}^{cr}$). d) Experimentally obtained buckled state of the representative geometries A–H.

4.3. Penalizing Higher Modes

To investigate whether mode switching influences the experimental post-buckling behavior of our optimized geometries, we next introduce a penalty in our optimization problem that enforces a minimum separation between the first and second critical buckling force. To do so, we rewrite the objective function from Equation (10a) as

$$\min_{\rho_i} \quad \Phi(\rho_i) = \sqrt{\left(\tilde{\lambda}_1 - \tilde{\lambda}_{1T}\right)^2} + \alpha \frac{\delta\tilde{\lambda} - \delta\tilde{\lambda}_T}{\delta\tilde{\lambda}_T} \quad (11)$$

in which α is the penalty factor, equal to

$$\alpha = \begin{cases} 1/5 & \text{if} \quad \delta\tilde{\lambda} < \delta\tilde{\lambda}_T \\ 0, & \text{if} \quad \delta\tilde{\lambda} \geq \delta\tilde{\lambda}_T \end{cases} \quad (12)$$

For further optimization studies we chose $\delta\tilde{\lambda}_T = \tilde{\lambda}_2 - \tilde{\lambda}_1 = 0.3$ as the minimum distance between the first and second buckling mode. Rerunning the previous optimization study now with the penalty applied to the buckling force of the second mode

has a considerable effect on the results. This becomes clear in Figure 6b, in which we show the difference between the buckling force $\delta\tilde{\lambda}$ for the optimized structures in function of the moment on inertia $\tilde{I}$. The sharp transition at $\tilde{I} \approx 3$ is still present; however, the results levels off for $\tilde{I} > 3$ at the specified minimum of $\delta\tilde{\lambda} = 0.3$. It is important to note that by using this penalty we only find structures that exhibit a macroscopic buckling mode with a wavelength of $2n_y^{uc}L$. Moreover, while we are still able to achieve structures similar to A–F found previously, **Figure 6**a shows that after the introduction of the penalty, we no longer observe clusters of structures with a microstructure similar to G and H (Figure 4a).

To asses whether the separation of the first and second mode has an effect on the buckling behavior of our structures, we fabricated two different geometries belonging to the F′ group, and used the same protocol as before to test them in a compression machine. In Figure 6c, we show the buckling modes of the optimized geometries F′₁ and F′₂ obtained using both simulations and experiments. While the designs are nearly identical to structure F (Figure 4), these structures undergo macroscopic buckling as predicted by our simulations before exhibiting a
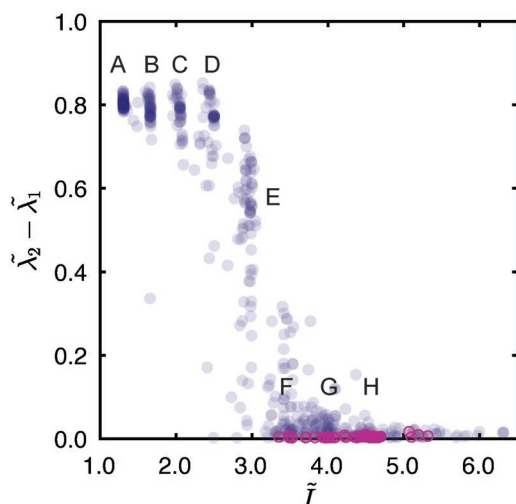
**ADVANCED
SCIENCE NEWS**

www.advancedsciencenews.com

**ADVANCED
FUNCTIONAL
MATERIALS**

www.afm-journal.de

Figure 5. Difference between the buckling load of the first and second mode $\tilde{\lambda}_2 - \tilde{\lambda}_1$ of the optimized structures from Figure 4, as a function of the moment of inertia $\tilde{I}$. Structures with first modes characterized by long ($2n_y^{uc}L$) or short ($2L$) wavelengths are indicated by the blue and pink markers, respectively.

creasing instability (see Figure S3b, Supporting Information). In fact, by adding the experimental results in terms of buckling force $\tilde{F}^{cr}$ to Figure 4c, we find that the structures exhibit the same geometrical stiffening as predicted. Therefore, we conclude that the second mode for structures F_1' and F_2' is separated well enough to prevent mode switching.

4.4. Maximum Mode Separation

Finally, to explore the maximum mode separation that can be achieved between the first two modes, we introduce a different objective function given by

$$\min_{\rho_i} \quad \Phi(\rho_i) = \sqrt{\left(\tilde{\lambda}_1 - \tilde{\lambda}_{1T}\right)^2 + \left(\tilde{\lambda}_2 - \tilde{\lambda}_{2T}\right)^2} \tag{13}$$

We ran a total of 2104 optimizations with target eigenvalues ranging between $\tilde{\lambda}_{1T} = [0.4, 2.4]$ and $\tilde{\lambda}_{2T} = [\tilde{\lambda}_{1T}, 3]$. In **Figure 7**, we show the results in terms of the optimized buckling forces $\tilde{\lambda}_1$ and $\tilde{\lambda}_2$. Interestingly, we find a bounded region of buckling behavior that can be achieved, indicated by the gray area. In fact, while we can optimize for structures with coincident critical points $\tilde{\lambda}_1 \approx \tilde{\lambda}_2$ resulting in so-called frustrated structures,[64] there is a maximum separation $\tilde{\lambda}_2 - \tilde{\lambda}_1$ which can be achieved. This value seems to be dependent on the $\tilde{\lambda}_1$, since for $\tilde{\lambda}_1 < 1$ the maximum separation achievable $\tilde{\lambda}_2 - \tilde{\lambda}_1 \propto \tilde{\lambda}_1$, and for $\tilde{\lambda}_1 > 1$, $\tilde{\lambda}_2 - \tilde{\lambda}_1 \propto \tilde{\lambda}_1 + 0.85$. These results are coherent with the results shown in Figures 5 and 6b. Therefore, the gray area shown in Figure 7 represents a projection of the design space onto the control variables of our inverse design problem.

5. Conclusions

In this work, we have applied stochastic optimization to tackle disjoint topology optimization problems. Furthermore, in order to create feasible optimized geometries, we proposed an Ising-inspired subroutine to effectively guide the optimization and cluster material. After testing our method and reproducing the results of a widely used, differentiable, compliance optimization problem, we approached optimization problems dealing with the buckling behavior of mechanical metamaterials. Specifically, in this paper, we focused on the optimization of the first two buckling modes of a beam and their interaction. While here we focused on the optimization of beams that exhibit 1D periodicity, our method can also be applied on structures with higher periodicities. For example, Figure S5, Supporting Information, demonstrates the optimization of a 2D lattice, with multiple load cases. As such, our method opens up new avenues for the exploration of more fundamental questions regarding frustration and mode interaction that occur in these and more complex mechanical metamaterials.

While in the current work the Ising energy has been defined by penalizing interfaces (i.e., acting effectively as a surface
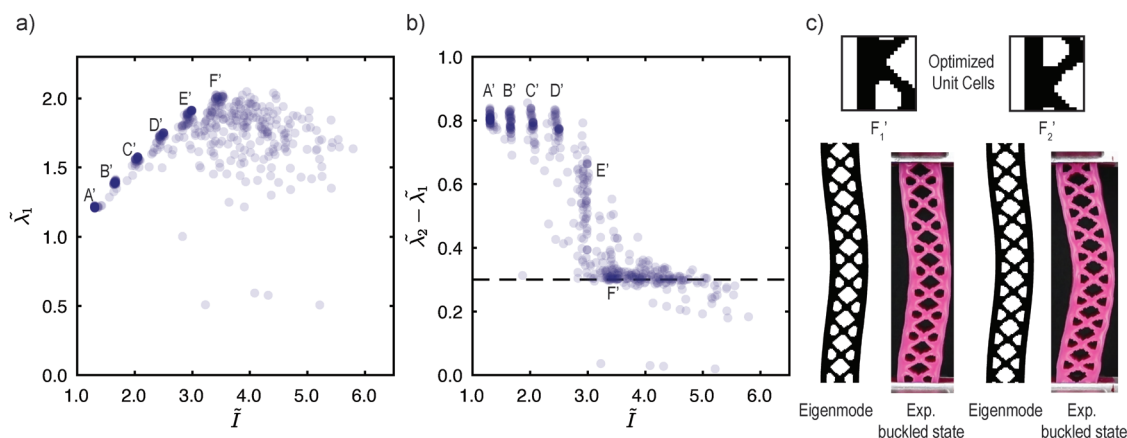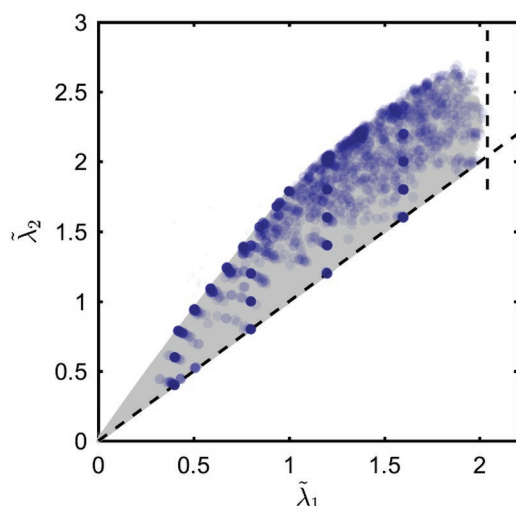

Figure 6. Maximum buckling load optimization with penalization of the second buckling mode according to Equation (11) with $\delta\tilde{\lambda}_T = 0.3$. a) Buckling load $\tilde{\lambda}_1$ of 600 optimizations in function of average moment of inertia $\tilde{I}$. Most of the results cluster in the same minima $A' - F'$ as previous maximization study without penalization; however, structures G and H are no longer present (Figure 4a). b) Difference between the buckling load of the first and second mode $\tilde{\lambda}_2 - \tilde{\lambda}_1$ as a function of the average moment of inertia $\tilde{I}$. c) Comparison between buckling modes obtained using simulations and experiments for two representative geometries belonging to cluster F'.

Figure 7. Optimization results for 56 different combinations of target buckling values ($\tilde{\lambda}_{1T}$, $\tilde{\lambda}_{2T}$), where $\tilde{\lambda}_{1T} = [0.4, 2.4]$ and $\tilde{\lambda}_{2T} = [\tilde{\lambda}_{1T}, 3]$. The blue markers indicate all optimized solutions, while the gray area shows all the evaluated solutions during the optimization, indicating the feasible design space for our optimization problem. The diagonal dashed lines represent the determined bounds, specified by $\tilde{\lambda}_1 = \tilde{\lambda}_2$, and $\tilde{\lambda}_1 < 2.1$.

tension) by reducing the probability of drawing these solutions, other energy potentials with longer range interactions or physics based potentials could be used to alter the candidate selection. This could potentially vary the minimum feature size or incorporate specific geometrical features in the final solution.

Moreover, because our method does not require objective function differentiability, it can be applied to different problems that would be impossible otherwise. These can range from optimization of the buckling shape of mechanical metamaterials or the band gap behavior of periodic and aperiodic photonic, and acoustic metamaterials, to their fully nonlinear, transient, and unstable behavior. Therefore, we believe that the flexibility and simplicity of our method is a good addition to existing gradient-based optimization problems, and is able to deal with more complex problems that have been left unexplored so far.

Supporting Information

Supporting Information is available from the Wiley Online Library or from the author.

Acknowledgements

Conflict of Interest

The authors declare no conflict of interest.

[1] D. R. Smith, J. B. Pendry, M. C. K. Wiltshire, *Science* **2004**, *305*, 788.
[2] J. B. Pendry, *Phys. Rev. Lett.* **2000**, *85*, 3966.
[3] R. Lakes, *Science* **1987**, *235*, 1038.
[4] X. Zheng, H. Lee, T. H. Weisgraber, M. Shusteff, J. DeOtte, E. B. Duoss, J. D. Kuntz, M. M. Biener, Q. Ge, J. A. Jackson, S. O. Kucheyev, N. X. Fang, C. M. Spadaccini, *Science* **2014**, *344*, 1373.
[5] T. Ergin, N. Stenger, P. Brenner, J. B. Pendry, M. Wegener, *Sciences* **2010**, *328*, 337.
[6] T. Bückmann, M. Kadic, R. Schittny, M. Wegener, *Proc. Natl. Acad. Sci. U. S. A.* **2015**, *112*, 4930.
[7] K. Bertoldi, P. M. Reis, S. Willshaw, T. Mullin, *Adv. Mater.* **2010**, *22*, 361.
[8] J. T. B. Overvelde, S. Shan, K. Bertoldi, *Adv. Mater.* **2012**, *24*, 2337.
[9] J. T. B. Overvelde, K. Bertoldi, *J. Mech. Phys. Solids* **2014**, *64*, 351.
[10] Z. Y. Wei, Z. V. Guo, L. Dudte, H. Y. Liang, L. Mahadevan, *Phys. Rev. Lett.* **2013**, *110*, 215501.
[11] J. T. B. Overvelde, T. A. De Jong, Y. Shevchenko, S. A. Becerra, G. M. Whitesides, J. C. Weaver, C. Hoberman, K. Bertoldi, *Nat. Commun.* **2016**, *7*, 10929.
[12] D. P. Holmes, A. J. Crosby, *Adv. Mater.* **2007**, *19*, 3589.
[13] J. Li, J. Shim, J. Deng, J. T. B. Overvelde, X. Zhu, K. Bertoldi, S. Yang, *Soft Matter* **2012**, *8*, 10322.
[14] K. Bertoldi, M. C. Boyce, *Phys. Rev. B* **2008**, *77*, 052105.
[15] P. Wang, J. Shim, K. Bertoldi, *Phys. Rev. B : Condens. Matter Mater. Phys.* **2013**, *88*, 014304.
[16] W-P. Yang, L-W. Chen, *Smart Mater. Struct.* **2007**, *17*, 015011.
[17] D. Terwagne, M. Brojan, P. M. Reis, *Adv. Mater.* **2014**, *26*, 6608.
[18] P-C. Lin, S. Yang, *Soft Matter* **2009**, *5*, 1011.
[19] J. Kim, J. Yoon, R. C. Hayward, *Nat. Mater.* **2010**, *9*, 159.
[20] B. Florijn, C. Coulais, M. Van Hecke, *Phys. Rev. Lett.* **2014**, *113*, 175503.
[21] J. Shim, S. Shan, A. Kosmrlj, S. H. Kang, E. R. Chen, J. C. Weaver, K. Bertoldi, *Soft Matter* **2013**, *9*, 8198.
[22] S. Shan, S. H. Kang, P. Wang, C. Qu, S. Shian, E. R. Chen, K. Bertoldi, *Adv. Funct. Mater.* **2014**, *24*, 4935.
[23] M. Philip Bendsøe, N. Kikuchi, *Comput. Methods Appl. Mech. Eng.* **1988**, *71*, 197.
[24] O. Sigmund, K. Maute, *Struct. Multidiscip. Optim.* **2013**, *48*, 1031.
[25] V. J. Challis, A. P. Roberts, A. H. Wilkins, *Int. J. Solids Struct.* **2008**, *45*, 4130.
[26] M. M. Neves, H. Rodrigues, J. M. Guedes, *Struct. Optim.* **1995**, *10*, 71.
[27] D. C. Dobson, S. J. Cox, *SIAM J. Appl. Math.* **1999**, *59*, 2108.
[28] O. Sigmund, J. S. Jensen, *Philos. Trans. R. Soc., A* **2003**, *361*, 1001.
[29] J. S. Jensen, O. Sigmund, *Appl. Phys. Lett.* **2004**, *84*, 2022.
[30] O. Sigmund, K. Hougaard, *Phys. Rev. Lett.* **2008**, *100*, 153904.
[31] S. Halkjær, O. Sigmund, J. S. Jensen, *Z. Kristallogr. - Cryst. Mater.* **2005**, *220*, 895.
[32] O. Sigmund, S. Torquato, *Appl. Phys. Lett.* **1996**, *69*, 3203.
[33] A. Clausen, F. Wang, J. S Jensen, O. Sigmund, J. A. Lewis, *Adv. Mater.* **2015**, *27*, 5523.
[34] H. Deng, L. Cheng, X. Liang, D. Hayduke, A. C. To, *Comput. Methods Appl. Mech. Eng.* **2020**, *358*, 112641.
[35] T. Borrvall, J. Petersson, *Int. J. Numer. Methods Fluids* **2003**, *41*, 77.
[36] X. Gao, H. Ma, *Comput. Struct.* **2015**, *157*, 142.
[37] C. R. Thomsen, F. Wang, O. Sigmund, *Comput. Methods Appl. Mech. Eng.* **2018**, *339*, 115.
[38] O. Sigmund, *Struct. Multidiscip. Optim.* **2011**, *43*, 589.
[39] P. Y. Shim, S. Manoochehri, *Int. J. Numer. Methods Eng.* **1997**, *40*, 1053.
[40] B. Baumann, B. Kost, *Comput. Struct.* **2005**, *83*, 2175.
[41] J. W. Rocks, N. Pashine, I. Bischofberger, C. P. Goodrich, A. J. Liu, S. R. Nagel, *Proc. Natl. Acad. Sci. U. S. A.* **2017**, *114*, 2520.
[42] C. P. Goodrich, A. J. Liu, S. R. Nagel, *Phys. Rev. Lett.* **2015**, *114*, 225501.

[43] D. V. Hinkley, D. R. Cox, *Theoretical Statistics*, Chapman and Hall/ CRC, London/Boca Raton, FL **1979**.

[44] D. Pihler-Puzović, A. L. Hazel, T. Mullin, *Soft Matter* **2016**, *12*, 7112.

[45] C. G. Johnson, U. Jain, A. L. Hazel, D. Pihler-Puzović, T. Mullin, *Proc. R. Soc. A* **2017**, *473*, 20170477.

[46] A. P. Seyranian, E. Lund, N. Olhoff, *Struct. Optim.* **1994**, *8*, 207.

[47] M. P. Bendsøe, *Struct. Optim.* **1989**, *1*, 193.

[48] M. P. Bendsøe, O. Sigmund, *Topology Optimization Theory, Methods, and Applications*, Springer, Berlin **2004**.

[49] S. Kirkpatrick, C. D. Gelatt, M. P. Vecchi, *Science* **1983**, *220*, 671.

[50] Y. Nourani, B. Andresen, *J. Phys. A: Math. Gen.* **1998**, *31*, 8373.

[51] N. Olhoff, M. P. Bendsøe, J. Rasmussen, *Comput. Methods Appl. Mech. Eng.* **1991**, *89*, 259.

[52] O. Sigmund, *Struct. Multidiscip. Optim.* **2001**, *21*, 120.

[53] O. Sigmund, J. Petersson, *Struct. Optim.* **1998**, *16*, 68.

[54] A. Diaz, O. Sigmund, *Struct. Optim.* **1995**, *10*, 40.

[55] O. Sigmund, *Design of Material Structures Using Topology Optimization, PhD Thesis*, Technical University of Denmark (Denmark) **1994**.

[56] T. A. Poulsen, *Struct. Multidiscip. Optim.* **2002**, *24*, 396.

[57] M. Rouhi, M. Rais-Rohani, T. N. Williams, *Struct. Multidiscip. Optim.* **2010**, *42*, 215.

[58] E. Ising, *Z. Phys.* **1925**, *31*, 253.

[59] S. G. Brush, *Rev. Mod. Phys.* **1967**, *39*, 883.

[60] B. Budiansky, *Adv. Appl. Mech.* **1974**, *14*, 1.

[61] S. P. Timoshenko, J. M. Gere, *Theory of Elastic Stability*, Courier Corporation, North Chelmsford, MA **2009**.

[62] S. C. Johnson, *Psychometrika* **1967**, *32*, 241.

[63] E. Hohlfeld, L. Mahadevan, *Phys. Rev. Lett.* **2011**, *106*, 105702.

[64] S. H. Kang, S. Shan, A. Košmrlj, W. L. Noorduin, S. Shian, J. C. Weaver, D. R. Clarke, K. Bertoldi, *Phys. Rev. Lett.* **2014**, *112*, 098701.